River Flow 2010 - Dittrich, Koll, Aberle & Geisenhainer (eds) - © 2010 Bundesanstalt für Wasserbau ISBN 978-3-939230-00-7

Three-dimensional modelling of a very large river; the Río Paraná

S.D. Sandbach, R.J. Hardy & S.N. Lane
Department of Geography, Durham University, Durham, UK

D.R. Parsons
School of Earth and Environment, University of Leeds, Leeds, UK

J.L. Best
Departments of Geology and Geography University of Illinois Urbana-Champaign, IL, USA

P.J. Ashworth & A.J.H. Reesink
School of the Environment and Technology, University of Brighton, Brighton, UK

M.L. Amsler & R.N. Szupiany
Universidad Nacional del Litoral, Facultad de Ingeniería y Ciencias Hídricas, Santa Fe, Argentina

A.P. Nicholas
Department of Geography, University of Exeter, Exeter, UK

O. Orfeo
Centro de Ecologia Aplicada del Litoral, Corrientes, Argentina

G.H. Sambrook Smith
School of Geography, Earth and Environmental Sciences, University of Birmingham, Birmingham, UK

ABSTRACT: Our current understanding of the world's largest rivers is limited due to the difficulties in obtaining detailed, spatially-distributed, flow and morphological data. Recent progress has been made in obtaining data-rich results using Computational Fluid Dynamic (CFD) models within smaller river reaches, but the application of CFD to large rivers has not been fully developed due to our inability to: *i*) design numerically-stable meshes for complex topographies, and *ii*) collect high resolution data appropriate for model boundary conditions.

Here, we test a new five-term mass-flux scaling algorithm to include bed topography over large spatial scales, where the discretised form of the mass and momentum equations are modified using a mass-flux scalling approach. Converged solutions were obtained using Reynolds-Averaged Navier Stokes (RANS) equations with a κ–ε RNG turbulence closure. Topographic and velocity data were collected for a 38 km reach in the Río Paraná, Argentina, to provide boundary conditions and validation data. The model results demonstrate the importance of topographic steering on determining flow structures in large rivers and the difficulties in objectively identifying coherent secondary flows.

Keywords: Computational Fluid Dynamics, Large Rivers, Secondary Circulation, Numerical Modelling

1 INTRODUCTION

We currently have limited knowledge about flow processes and sediment transport in large rivers that are characterised by high width to depth ratios (Lane et al. 2008). A growing body of evidence suggests that our understanding of flow processes gained from smaller rivers is not always transferable to larger rivers.

Richardson & Thorne (1998) investigated the velocity field around a braid bar in the Brahmaputra River using aDcp measurements. Their preliminary results indicate that some flow patterns were consistent with features observed in bends of smaller scale single-thread meandering channels. Viscardi et al. (2006) investigated the flow in a branch of the Paraná de las Palmas. Their results indicate the presence of secondary circulatory flow in the San Antonio bend.

However more recent aDcp measurements obtained in the Río Paraná (Parsons et al. 2005; 2008; Lane et al. 2008) suggest that some of the classical flow processes operating in smaller rivers are absent in larger rivers. Parsons et al. (2008) found that channel-scale circulation, commonly associated with mid-channel bars, was absent and attributed this to the greater influence of form roughness as the width-depth ratio increased. Only where a large confluence influenced the generating mechanisms of flow structure, for example at the Río Paraguay - Río Paraná junction, was

channel-scale circulation observed (Lane et al. 2008).

Obtaining field measurements of very large rivers is both expensive and difficult due to the scales involved. For this reason, numerical modelling offers an appealing alternative as it permits a much more detailed investigation of flow structure and processes that would otherwise not be possible with current field techniques.

However, modelling fluvial flows presents us with two major difficulties: *i*) the need for high-resolution data to provide physically realistic boundary conditions and *ii*) an appropriate numerical methodology to include variations in bed topography. Recent advancements in both field-based techniques and CFD methodologies for fluvial flows have provided: *i*) a means to measure bed topology and the velocity field (cf. Parsons et al. 2005) and *ii*) to represent these flows in a numerically-stable manor (Olsen & Stokseth 1995; Lane et al. 2004; Hardy et al. 2006). In this paper, we utilise these advancements to investigate flow structures in a very large river: the Río Paraná.

2 METHODOLOGY

2.1 *Mass Flux Scaling Method*

Here we adopt a mass-flux scaling method to include topographic variations in river bed morphology. This method has been developed and validated for high-resolution applications (Lane et al. 2004) to include complex topography (individual gravel particles) at small (0.002 meters) spatial scales. More recently, this method has been used to investigate larger-scale flows (Hardy et al. 2006) over a dune field (1.8 km by 0.25 km) in the Río Paraná. In this paper, we investigate further the use of these methods at very large scales using data obtained over a ~38 km reach in the Río Paraná.

The method is based on a mass-flux scaling methodology, similar to that of Olsen & Stokseth (1995), which used a structured grid specifying cell porosities to block out the bottom topography (P_f =1 for cells that are all water, P_f =0 for cells that are all bed and $0<P_f<1$ for partly blocked cells) with appropriate drag terms introduced into the momentum equations (Lane et al. 2004). In the present paper, a modified version of this method is applied with a five-term mass-flux scaling algorithm that includes four vertical faces of the cell and the cell volume rather than a single scaling term (Hardy et al. 2006).

2.2 *Field Campaign*

Alongside the model development, a field study was undertaken to collect flow and topographic data required to provide both boundary conditions and validation data for the numerical model. Throughout the reach, a combined bed topography and three-dimensional flow survey was conducted from two research vessels.

The topographic data was obtained (Figure 1) using a RESON Navisound 215 dual frequency (33 and 210 kHz) single-beam echo-sounder (SBES) collecting data at ~1 Hz linked to a global positioning system (GPS). This topographic information was collected at 163 cross-sections separated by approximately 200 m in the downstream direction and a series of longitudinal lines along the length of the reach. The surveyed lines were projected to a UTM co-ordinate system and post-processed in CARIS HIPS software, where the effect of changing stage over the survey was corrected. The final survey points were exported to ArcMap to generate a Digital Elevation Model (DEM). A kriging algorithm was applied to interpolate the data to a 50*50 m grid. Co-location of the flow and topographic data was achieved using a Leica RTK GPS.

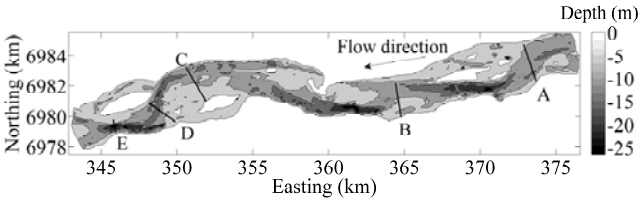

Figure 1. Digital Elevation Model of the 38 km reach studied with the location of the aDcp cross-sections (A–E) indicated.

The flow data were obtained using an RDI 1200 kHz (aDcp), which determines three-dimensional flow in a vertical column at 0.25 m interval bins. The aDcp was deployed in moving-boat mode with vessel and velocity correction provided via RTK GPS. A total of five cross-sections through the reach were measured. Following recommendations in Szupiany et al. (2007), at each section, six repeat transects were collected to obtain a statistically-stationary flow field. Average boat velocity during the aDcp surveys was 1.12 m s^{-1}, providing high-resolution (~1 x 4 samples m^{-2}) velocity data through each cross-section. The distance from the water surface to the first bin was 0.74 m, which accounted for submergence of the aDcp below the waterline and the blanking distance that removes the effect of sidelobe ringing. Data from the bottom 6% of the profile was removed in processing, again to remove the effect of contamination by sidelobe interference.

2.3 *Model Set-up*

The aDcp data from cross-section A (Figure 1) was used to orientate the DEM relative to the computational mesh; *y* and *z* were parallel to, and *x* perpendicular to, the cross-section (Figure 2) and the flow data from this cross-section was then used as an inlet boundary condition (a fixed mass boundary). The outlet was defined on the opposite end of the domain using a fixed-pressure boundary condition where mass is allowed to enter and leave the domain.

The simulations were undertaken on a Cartesian mesh using the PHEONICS© finite volume code. Pressure was computed using the SIMPLE (Patankar & Spalding 1972) algorithm and the hybrid differencing scheme (Spalding 1972) was employed to compute convective terms. The rigid lid approximation was applied at the free-surface with the no slip condition applied at the bed.

The origin of the Cartesian co-ordinate system in the horizontal plane was selected so that *x* and *y* were everywhere greater than or equal to zero. In the vertical, the water surface provides the vertical datum (z=0) with depths assigned negative values. The results presented in this paper utilise the depth measurements obtained at the time of survey and so they are specific to that stage.

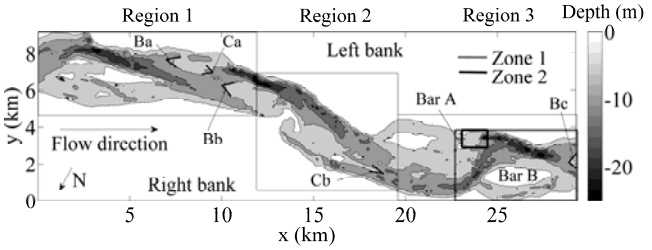

Figure 2. The rotated DEM with the regions modelled and zones investigated indicated.

Computational constraints limited the maximum domain size to approximately 6.3 million finite volume cells. For the reach scale investigated here (38 km long and 2–4 km wide), it was not possible to model the entire reach using a single simulation. We therefore employed a multi-region method where *n* regions were modelled systematically. Converged solutions for each region were obtained within two weeks with the solved flow variables from the outlet face used to supply the next region of the reach with inlet boundary conditions. Following this procedure for the remaining regions, the entire reach was modelled.

To determine the suitable cell dimensions we have employed the global convergence index (GCI: Hardy et al. 2003) to test for mesh independence. These tests were employed on a smaller reach with the topography removed to eliminate the effects of spatial interpolation of topography. The GCI method involves a series of grid refinements where the finite volume dimensions are reduced by a factor of two with at least three domains used to assess the solution convergence. In these simulations, the mesh size was set to 15 m in the horizontal plane (Δ_x and Δ_y) and 1 m in the vertical direction (Δ_z). Using the method outlined above, three regions were required to model the entire reach and details of the mesh dimensions used are provided in Table 1.

Table 1. Mesh dimensions used in the simulations

Region	N_x	N_y	N_z
1	775	297	26
2	550	439	26
3	628	292	26

3 RESULTS

3.1 *Primary Flow*

The flow at the free surface for the entire reach is presented in Figure 3 and is represented using a series of streamlines. The streamlines commence 100 m downstream of the inlet and are separated by 250 m in the cross-stream direction and are plotted superimposed on the bed topography for reference. The streamline pattern illustrates the dominance of the thalweg in controlling the direction of the primary flow and the pronounced level of convergence and divergence of the flow field throughout the reach:

i) In the uppermost part of the reach, the thalweg extends across most of the river (Figure 3). The mean direction of the thalweg through this zone is approximately 45° to the main channel axis and the flow at the free surface is largely parallel to the thalweg. Approximately 70% of the flow that enters the reach at the free surface follows the thalweg to the left of the bar complex (Figure 3, labelled a).

ii) Further downstream, the flow is forced to diverge upstream of the submerged bifurcation Bb (Figure 3, labelled b).

iii) In the middle of the reach, there is a significant convergence of the streamlines through a zone of thalweg curvature (Figure 3, labelled c). After this convergence, most of the flow at the free surface continues to follow the thalweg. However, a portion (~20%) diverges to the right bank, driven in part by an incipient, or submerged, bar in the central zone of the channel and a deeper portion of the channel, which is probably a former thalweg (Figure 3).

iv) In the lower part of the reach there is a convergent-divergent section of the thalweg (Figure 3, labelled d). The flow at the free surface follows

the same pattern as the thalweg bed topography through this region of convergence and divergence.

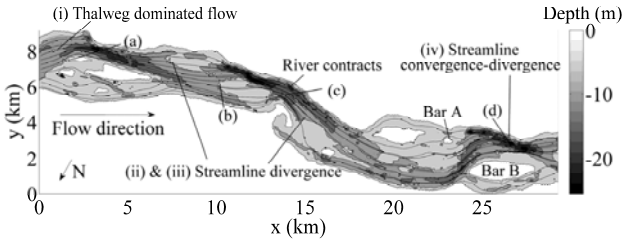

Figure 3. Free surface streamlines and topographic data.

In zone 1 (Figure 2), the thalweg follows a sinuous path. In the upstream part of this zone, the thalweg moves out towards the left bank in front of bar B at approximately 45° to the downstream direction with the thalweg width increasing, before converging and curving back to follow primarily the main channel direction.

To investigate the primary flow in this zone, an array of streamlines and contour slices of the divergence angles are presented in Figure 4. The streamlines commence at the upstream face of the zone, separated by 20 m in the cross-stream direction and 2 m in the vertical. This set of curves represents the primary flow direction since by definition they are tangential to the velocity field at all points along each streamline.

The flow is topographically steered, primarily by the thalweg. Flow in the upstream part of the channel is forced to diverge with most of the flow diverted towards the left bank. Further along the thalweg, curvature of the thalweg forces the flow back towards the main channel direction. Towards the end of this zone, the submerged bifurcation Bc forces the flow to diverge. The flow in the shallower (~4 m deep) upstream part of this zone converges with the thalweg. The dominance of the thalweg is clearly evident as the flow is forced laterally (at x~23 km).

Also included in Figure 4 are downstream slices representing the divergence angle θ $(=\tan^{-1}(u_y/u_x))$ at constant cross-stream locations (y=370, 800, 1500, 2100 and 3300 m) for the entire zone. This angle represents the primary flow direction relative to the x-axis where: $\theta = 0^o$, the flow is moving downstream; $\theta = 90^o$, the flow is directed towards the left bank and; $\theta = -90^o$, the flow is directed towards the right bank.

Flow in the thalweg upstream of bar B is characterised by contour slice SL2 (see label a). The flow in this region is topographically steered a significant distance upstream (~1 km) of bar B with the divergence angle increasing by approximately 20° (flow towards the left bank). Further along the thalweg, the flow is forced further laterally with the divergence angle increasing to approximately 45° by contour slice SL3 (see label b, approximately the same position as the thalweg).

Further along the channel, the thalweg width increases significantly with the margins extending across stream and downstream (along bar B). Contour slices SL4–SL6 characterise the flow in this expanding region along with the streamline representation. Here the flow moves out into the expanding region, and is further topographically steered downstream into a contraction in width followed by a subsequent divergence upstream of submerged bifurcation Bc (Figure 2).

In the upstream part (slice SL4), the divergence angle is approximately 40° (see label c) and this is reduced further downstream to approximately 0°

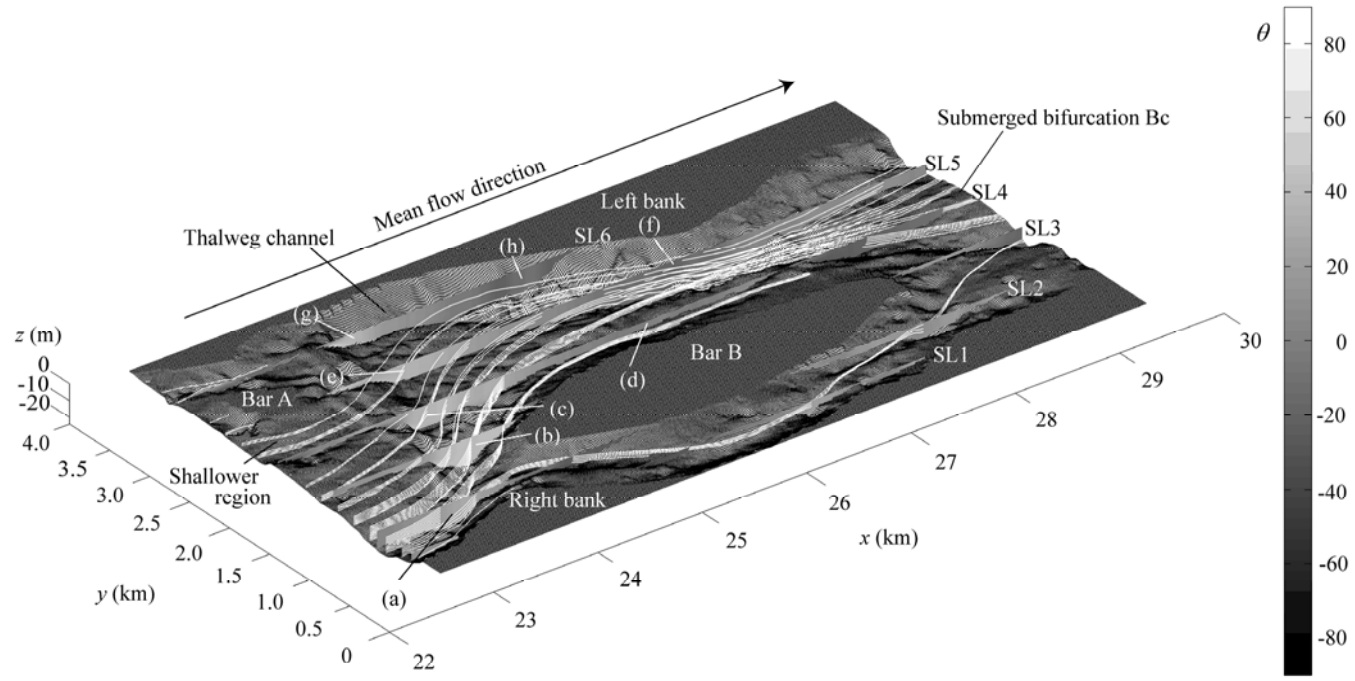

Figure 4. The flow in zone 1 represented using slices of the divergence angles and a series of streamlines.

(see label d), implying predominately downstream axial flow through this zone. In the remaining contour slices SL5 and SL6, similar flow patterns are evident although in the downstream part of each slice (upstream of the contraction), the divergence angle is reduced further (~-20°, see f & h). At the upstream end of contour slice SL5, the divergence angle is approximately 35° (see label e). This reduction in divergence angle (see labels c & e) is caused by thalweg curvature in the downstream axial direction. However, in the upstream portion (SL6), there is an increase in the divergence angle (~45°, see label g) as compared to SL4 & SL5 (~35°–40°, see labels e & g). The flow in this region is driven by the thalweg scour close to the left bank in zone 1. This further illustrates the dominance of the deeper channels, such as the thalweg and scours, in controlling the primary flow direction throughout the reach.

3.2 *Secondary Flow*

Using current methodologies to separate the primary and secondary flow, a single planar surface that extends across the entire reach is typically used (cf. Dietrich & Smith 1983). The flow parallel and perpendicular to this plane is defined as secondary and primary flow respectively. However, in regions where the flow converges (e.g. downstream of a confluence), the use of a single planar surface can be misleading. Lane et al. (2000) suggest that these methods should be applied in two parts on either side of the confluence mixing layer, although this provides difficulties in defining the 'hinge point' as the mixing layer becomes more diffuse downstream of the junction (Lane et al. 2000). Similar methods are yet to be developed for divergent flow (e.g. upstream of a bifurcation) where the identification of a 'hinge point' is unclear.

In Figure 5, the topographic data from zone 1 has been annotated with arrows to depict the general flow patterns. In some areas of this zone, the application of a single planar surface is certainly questionable as the primary flow direction can change significantly within the section. Towards the end of this zone, one cross-section (labelled CS) is identified (Figure 5). Applying a single planar cross-section here (*i*) is clearly misleading since the flow is both convergent and divergent. Following the suggestions proposed by Lane et al. (2000), it is possible to construct two planar surfaces downstream of bar B (*ii*). In the same way, a third planar surface (*iii*) is perhaps desirable since the flow diverges upstream of the submerged bifurcation (Bc).

An obvious question therefore arises: how many planar surfaces are required to sufficiently represent the secondary and primary flow? This is dependent on both the scale of the flow investigated and the topographic steering of the flow to converge/diverge. Currently, we lack methods required to answer fully these questions and identify the necessary hinge points and planar surfaces. However, it appears a scale separation can be made between very large rivers where multiple planar surfaces are required and smaller channels where one or two planar surfaces are sufficient.

Therefore, herein we present unrotated cross-sectional velocity profiles and rely instead on the ability to take sections and desired orientations from the computational domain. In Figure 6, a series of cross-sections are presented in the upstream part of zone 1 (Figure 2) at x~24 km and y~3.5 km separated by 75 m in the downstream direction. Downstream velocity u_x is presented as contours with the cross-stream velocity u_y and u_z using a series of vectors. The flow in this region is characterised by the mixing between the flow in the deep thalweg and the shallower flow upstream. Such mixing is typically observed in post-confluence flow. However, here there is no distinct boundary separating the two streams and so the mixing layer is somewhat difficult to identify, adding further complexity to the identification of secondary flow.

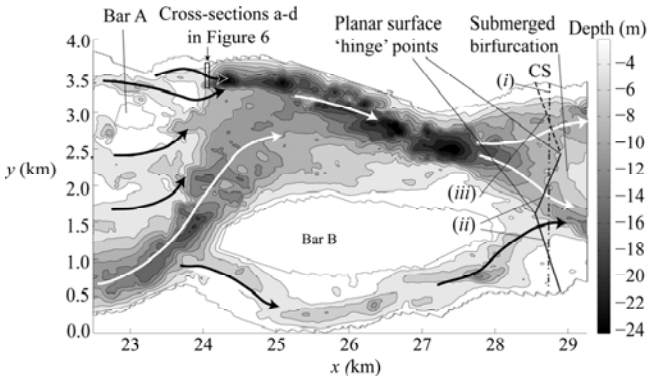

Figure 5. Schematic representation of the flow in zone 1.

The primary flow direction changes significantly across the 500 m wide cross-sections most notably in cross-sections a & b (Figure 6). The flow in these cross-sections is dominated by the momentum of the respective converging flow fields. The unit momentum ratio $R_M (= M_{tw}/M_{us} \sim 4)$, between the flow in the thalweg (M_{tw}) and in the upstream shallower region (M_{us}) shows that the thalweg is dominant. This ratio further increases downstream as the local flow depth increases, this is evidenced further downstream (see cross-sections c & d in Figure 6) where the flow becomes more uniform.

Although the velocity field in these cross-sections has not been resolved into primary and secondary flow, there is clearly evidence of cohe-

rent secondary circulation (see annotations in Figure 6). At y~3.4 km, three cells are evident where: *i*) the flow at the free surface is driven by the upstream topography; *ii*) the central flow is driven by convergence of the two streams and; *iii*) flow at the bed is driven largely by the thalweg. This circulation pattern is evident in all four cross-sections and is restricted to relatively narrow portions of the channel width in the deeper thalweg sections, similar to the results presented by Szupiany et al. (2009).

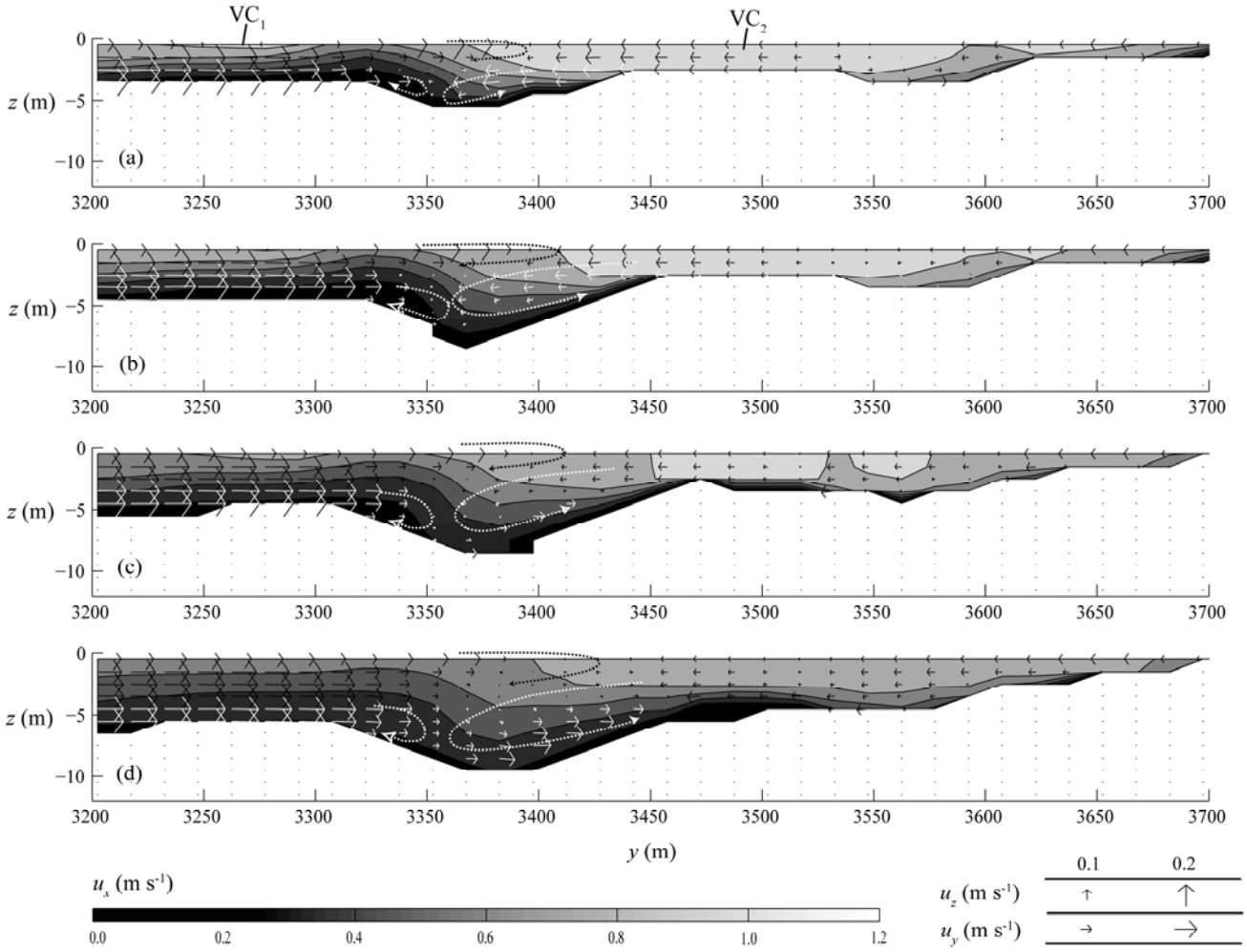

Figure 6. Contours of downstream velocity u_x and vector plots of the cross-stream and vertical velocity u_y and u_z.

In cross-section a, two cores of velocity (VC_1 & VC_2) are located at y~3.25 km and 3.8 km. Here, the downstream velocity (u_x) is an order of magnitude larger than the cross-stream velocity (u_y) and the momentum of the shallower upstream flow is dominant. Further downstream, this dominance is reduced due to mixing and reduced total momentum (depth expansion). Furthermore, since the total momentum depends on both velocity and cross-sectional area ($M \propto \int u^2 dA$), the length scale over which VC_1 dominates is significantly less than VC_2.

Although it is possible to build a picture of these flow patterns, we have not been able to separate the primary and secondary flow due to the increased length-scales. Stream-ribbons offer the possibility of visualising these secondary flow structures in strongly three-dimensional flows.

Stream-ribbons are an extension of streamlines. Each ribbon has a finite lateral extent and there trajectory through the domain is defined following the same principles as streamlines. The ribbons are twisted about the centre streamline to project secondary circulation. Twist of the ribbons is proportional to the local vorticity and a graduated contour of the integrated vorticity (χ) is used to further visualise secondary flow structure. The streamline integral of vorticity is defined:

$$\chi = \tfrac{1}{2}\int_S \frac{1}{u_p}\left(\frac{\partial u_{s,1}}{\partial x_{s,2}} - \frac{\partial u_{s,2}}{\partial x_{s,1}}\right) dx_p,$$

for streamline S where u_p and u_s are the primary and secondary components of velocity, x_p and x_s are the corresponding Cartesian co-ordinates where $x_{s,1}$ is perpendicular to $x_{s,2}$ (the convention here is the right-hand rule). Since the rate of change of χ with respect to stream-ribbon length (dS) is by definition the local vorticity, this contour provides a more quantitative measure of the local circulatory flow.

The stream-ribbons shown in Figure 7 represent flow in zone 2 (see Figure 2), with the topography also included as a surface plot. The ribbons commence at the upstream face (x~23.2 km) and are separated in the cross-stream and vertical directions by 70 and 3 m respectively. For direct cross-reference with the velocity plots (Figure 6), the locations of the first and last cross-sections are indicated. With this upstream perspective adopted, a counter-clockwise rotation of the flow results in an increase in χ.

In the upstream part of this zone, there is a channel formed between bar A and the left bank with lateral expansion in the downstream axial direction. This channel expansion drives streamline curvature of the flow locally. The flow close to bar A is forced river-right and the flow close to the left bank is forced river-left. Further downstream, there is a significant increase in depth as the flow that moved through this channel converges with the thalweg. Due to the dominance of the thalweg, the converging flow is forced laterally towards the left bank. This streamline curvature can be seen from inspection of Figure 7, where the flow is represented using a series of stream-ribbons.

These stream-ribbons indicate that secondary flow structures are generated throughout this zone. This secondary flow is apparently generated by streamline curvature driven locally by larger scale topography:

i) For stream-ribbon SR1, the flow is: (a) driven initially to the right due to channel expansion in the lee of bar A and; (b) subsequently forced left by the dominant thalweg. A corresponding change in vorticity is observed due to the change in curvature: (a) χ is initially reduced (clockwise circulation) followed by (b) an increase in χ (counter-clockwise circulation).

ii) A similar flow pattern is observed for stream-ribbon SR2. On approaching the thalweg, the flow is forced river-right (c) with a corresponding reduction in χ (counter-clockwise circulation). The dominant thalweg again forces the flow river-left (d) resulting in an increase in χ (clockwise circulation).

iii) Stream-ribbon SR3 shows a different flow pattern. In a similar way to stream-ribbon SR2, there is very little change in χ in the shallower

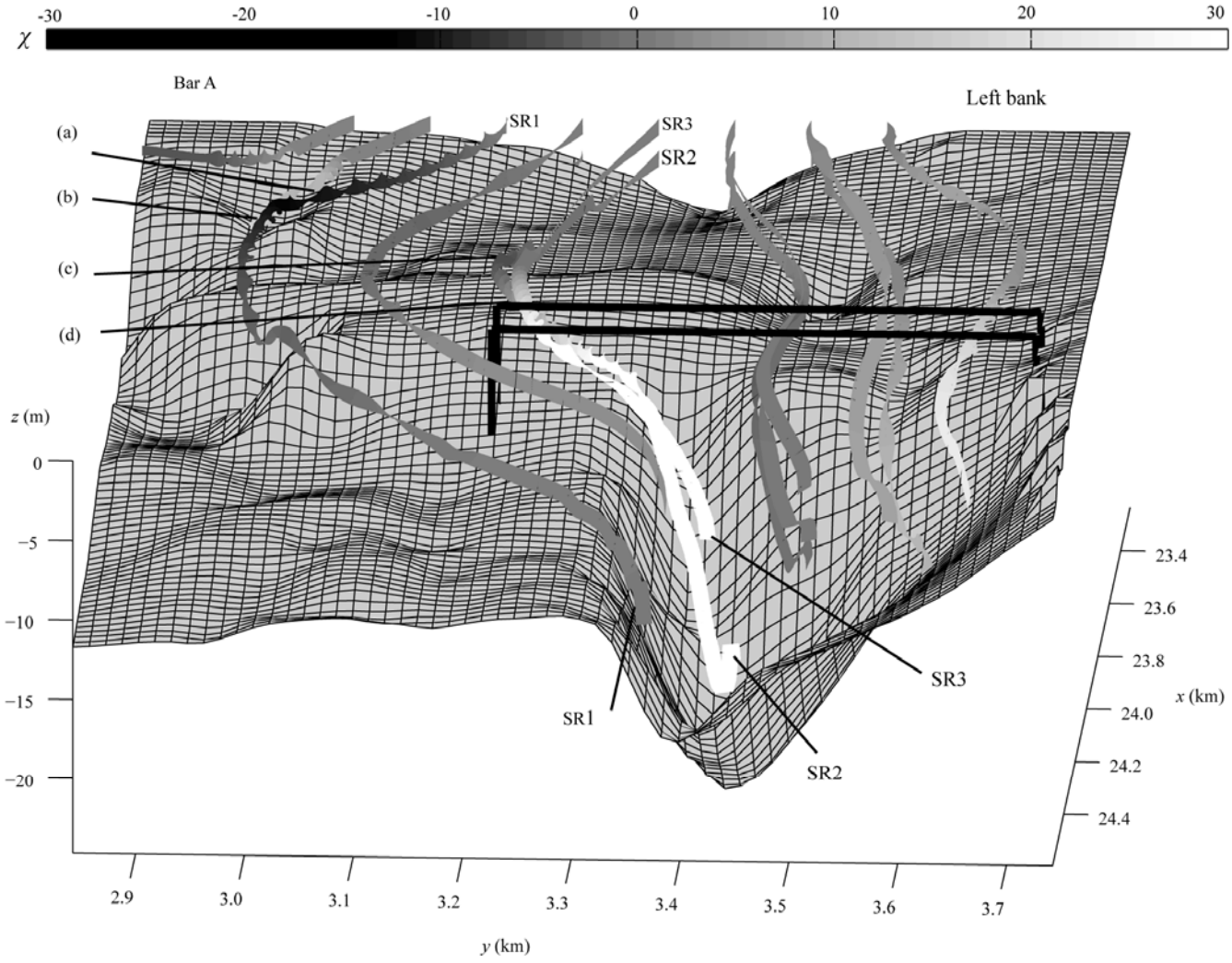

Figure 7. Stream-ribbon representation of the flow in zone 2.

upstream region. However, as the flow converges into the thalweg, the stream-ribbon indicates that flow is forced laterally towards the left bank. Convergence into the thalweg results in an increase in χ (counter-clockwise), again driven by the same mechanism.

Further inspection of ribbons SR2 and SR3, it is possible to see that the effects of topography on flow close to the bed are significantly larger than close to the free surface. Since these stream-ribbons pass through the velocity cross-sections shown in Figure 6, it is apparent that the downstream velocity near the free surface is an order of magnitude larger than the cross-stream velocity (VC_1, see Figure 6). Conversely, the downstream velocity near the bed is significantly smaller than the cross stream velocity.

4 CONCLUSIONS

In this paper we presented predictions of the three-dimensional flow structure in one of the world's largest rivers, the Río Paraná, obtained through the application of a CFD model. These results show that the large-scale topography dominates in steering the primary flow direction. At the reach scale, it appears that the flow direction is primarily driven by the deep thalweg channels, but locally observed free surface divergence and convergence is a result of topographic steering by larger scale barforms which are found throughout the reach.

These topographic controls drive streamline curvature that provides a mechanism to generate secondary flow, and there is clear evidence of coherent secondary circulation in the three-dimensional flow fields. However, such streamline curvature is driven locally rather than at the channel scale resulting in localised secondary flow structures.

Our research highlights some of the difficulties in objectively determining secondary flows at large spatial scales, and the need for improved methodologies to fully investigate 3D flow evolution in large rivers. One approach that appears to provide an insight into the secondary flow has been the application of stream-ribbons.

The application of the multi-region method has permitted a very large reach to be modelled. However, numerical inaccuracies associated with this method could lead to potential errors associated with matching a constant pressure outlet boundary with the inlet boundary of the following region. This could lead to propagation of error through the subsequent regions. We are currently validating these results with aDcp data and the initial comparisons are encouraging.

ACKNOWLEDGEMENTS

The authors are grateful to the Natural Environment Research Council for their financial support (NE/E016022/1) and the staff of CECOAL-CONICET (Corrientes, Argentina) for their essential field support in particular, Lolo Roberto and Rocce Negro.

REFERENCES

Dietrich, W.E, Smith, J.D. 1983. Influence of the point bar on flow through curved channels. *Water Resour Res*, 19(5), 1173-1192.

Hardy, R.J., Lane, S.N., Ferguson, R.I., Parsons, D.R. 2003. Assessing the credibility of a series of computational fluid dynamic simulations of open channel flow. *Hydrol Process*, 17(8), 1539-1560; DOI: 10.1002/hyp.1198.

Hardy, R.J., Parsons, D.R., Best, J.L., Lane, S.N., Kostaschuck, R., Orfeo, O. Three-dimensional modelling of flows over a natural dune field. *In: Ferreria, R.M.L., Alves, E.C.T.L., Leal, J.G.A.B., Cardos, A.H, River Flow 2006, London.: Taylor and Francis Group*, 1077-1083.

Lane, S.N., Bradbrook, K.S., Richards, P.M., Biron, P.M., Roy, A.G. 2000. Secondary circulation cells in river channel confluences: measurement artefacts or coherent flow structures?. *Hydrol Process*, 14, 2047-2071.

Lane, S.N., Hardy, R.J., Elliot, L., Ingham, D.B. 2004. Numerical modeling of flow processes over gravelly surfaces using structured grids and a numerical porosity treatment. *Water Resour Res*, 40(1); DOI: 10.1029/2002WR001934.

Lane S.N., Parsons, D.R. Best, J.L., Orfeo, O., Kostaschuk, R., Hardy, R.J. 2008. Causes of rapid mixing at a junction of two large rivers: Río Paraná and Río Paraguay, Argentina. *J Geophys Res*, 113(F2), DOI: 10.1029/2006JF000745.

Olsen, N.R.B. Stokseth, S. 1995. Three-dimensional numerical modelling of water flow in a river with large bed roughness. *J Hydraul Res*, 33(4), 571-581.

Parsons, D.R. Best, J.L., Orfeo, O., Hardy, R.J., Kostaschuk, R., Lane, S.N. 2005. Morphology and flow fields of three-dimensional dunes, Río Paraná, Argentina: Results from simultaneous multibeam echo sounding and acoustic Doppler current profiling. *J Geophys Res*, 110(F4), DOI: 10.1029/2004JF000231.

Parsons, D.R. Best, J.L., Lane, S.N., Orfeo, O., Hardy, R.J., Kostaschuk, R. 2008. Form roughness and the absence of secondary flow in a large confluence-diffluence, Paraná river, Argentina. *Earth Surface Processes and Landforms*, 32(1), 155-162, DOI: 10.1002/esp.1457.

Patankar, S.V., Spalding, D.B. 1972. A calculation procedure for heat, mass and momentum transfer in three-dimensional parabolic flows; *Int. J Heat Mass Transfer*, 15, 1787.

Richardson, W.R., Thorne, C.R. 1998. Secondary currents around braid bar in Brahmaputra river, Bangladesh. *J Hydraul Eng,* 124(3), 325-328; DOI: 10.1061/(ASCE)0733-9429(1998)124:3(325).

Spalding, D.B. 1972, A Novel Finite-Difference Formulation for Differential Expressions Involving Both First and Second Derivatives, *Int. J Num, Methods Eng*., 4, 551-559.

Szupiany, R.N., Amsler M.L., Best, J.L., Parsons, D.R. 2007. Comparison of fixed- and moving-vessel flow measurements with an aDp in a large river. *J Hydraul Eng,* 133(12), 1299-1309, DOI: 10.1061/(ASCE)0733-9429(2007)133:12(1299).

Szupiany, R.N., Amsler, M.L., Parsons, D.R., Best, J.L. 2009. Morphology, flow structure, and suspended bed sediment transport at two large braid-bar confluences. *Water Resour Res*, DOI: 10.1029/2008WR007428.

Viscardi, J.M., Pujol, A, Weibrecht, V., Jirka, G.H., Olsen, N.R. Numerical simulations on the Paraná de las Palmas River. *In: Ferreria, R.M.L., Alves, E.C.T.L., Leal, J.G.A.B., Cardos, A.H, River Flow 2006, London.: Taylor and Francis Group*, 367-377.